OEA | Opto-Electronic Advances

Article

March 2026, Vol. 9, No. 3

Open Access

Perovskite nanocrystals in glass for high efficiency and ultra-high resolution dynamic holographic multicolor display

Chao Ruan[1], Xinkuo Li[1], Ke Sun[2], Jianrong Qiu[1] and Dezhi Tan[1]*

Abstract: Incorporating perovskite nanocrystals (PNCs) in the glass matrix has been demonstrated to be an effective route to improve their stability for long-term operation. However, simultaneously achieving high luminance and high photoluminescence (PL) quantum yield (QY) is challenging. Herein, we report a strategy that employs fluoride ion doping to modify the three-dimensional glass network, thereby optimizing the crystallization behavior of PNCs and achieving both high luminance and high PLQY in full-spectrum. Leveraging these high-performance transparent composites, we constructed a dynamic holographic multicolor display system by integrating with a spatial light modulator (SLM), achieving a pixel density as high as 20,247 pixels per inch (PPI). We further propose a vertically stacked, multilayer full-color display architecture that overcomes the limitations of color filters in light-utilization efficiency and the bottlenecks of conventional planar sub-pixel layouts in terms of spatial utilization and resolution.

Keywords: perovskite nanocrystals; glass matrix; high efficiency photoluminescence; ultra-high resolution; multicolor display

DOI: 10.29026/oea.2026.250238 | CSTR: 32247.14.oea.2026.250238

Citation: Ruan C, Li XK, Sun K et al. Perovskite nanocrystals in glass for high efficiency and ultra-high resolution dynamic holographic multicolor display. *Opto-Electron Adv* **9**, 250238 (2026).

1 Introduction

Nanocrystals (NCs) play a pivotal role in the advancement of new generation displays, owing to their high luminescence efficiency, widely tunable optical properties, and a narrow emission bandwidth, driving the development of modern information display technologies[1–4]. Although NCs have been extensively integrated into displays such as liquid crystal displays (LCDs), Quantum Dots light-emitting diodes (QLEDs), and wearable displays, LCDs still suffer from high power consumption and low contrast[5–7], while QLEDs have limitations in reducing manufacturing costs and meeting high-resolution requirements[8–13]. Luminance and efficiency are core indicators for evaluating the performance of displays[14].

Recently, all-inorganic lead halide PNCs have been considered as ideal candidates for displays because of their outstanding PL properties[15,16], their bottleneck to commercialization is inherent environmental instability and the absence of efficient, pure-blue emitters[17–19]. Embedding $CsPbX_3$ (X=Cl, Br, I) PNCs within an inorganic glass matrix has emerged as an effective strategy to overcome this stability issue[20,21]. However, simultaneously achieving high luminance and high PL quantum efficiency is still challenging due to the strong self-absorption.

Dynamic holographic display has been the one of typical techniques for information and image display. Lasers with various wavelengths are generally necessary for the multicolor display. This is commonly achieved through methods such as rapidly switching between different colored lasers or combining the light modulated by several SLMs, which increases the system complexity and cost[22,23]. Recently, dynamic holographic display has been demonstrated by combining the computer-generated holography (CGH) and luminescent PNCs patterns, which inspires a new dynamic holographic display with single excitation wavelength[24]. A tight focusing holographic network has been established, which enables fast hologram computation and 3D real time

Received: 9 September 2025

Accepted: 16 December 2025

Published online: 24 February 2026

[1]State Key Laboratory of Extreme Photonics and Instrumentation, College of Optical Science and Engineering, and School of Materials Science and Engineering, Zhejiang University, Hangzhou 310027, China; [2]China International Science & Technology Cooperation Base for Laser Processing Robotics, Wenzhou University, Wenzhou 325035, China.
*Correspondence: Tan DZ, E-mail: wctdz@zju.edu.cn

accurate light field modulation for dynamic displays[25]. However, display resolution is limited and dynamic holographic multicolor display is still difficult due to the relatively low PLQY of the PNCs in glass.

In this work, NaF doping was employed to depolymerize the glass network and improve $CsPbX_3$ crystallization, enhancing the PLQY of full-spectrum PNCs in glass. A high resolution dynamic holographic display system was demonstrated with a pixel density up to 20,247 PPI. A notable breakthrough in this display technology was realized by utilizing sequentially stacked layers of multicolor emissive glass, enabling multilayer and multicolor fluorescent pixel excitation.

2 Results and discussion

The concurrent realization of high luminance and high PLQY in luminescent glasses represents a significant challenge due to the strong self-absorption, but it remains a crucial objective for their practical application in optoelectronics[26–28]. In this study, a series of borosilicate glass precursors co-doped with various perovskite constituents and fluorine were prepared through a conventional melt-quenching technique. Through subsequent stress-relief annealing and a controlled heat-treatment, PNCs were successfully grown in situ within the glass matrix. By precisely tuning the stoichiometric ratio of Pb, X (X=Cl, Br, I), and F, continuous spectral tunability was achieved nearly across the entire visible spectrum, spanning from the blue region (~459 nm) to the red region (663 nm) (Fig. 1(a)).

Guided by synchronous thermal analysis (STA) curves (Fig. S1), an appropriate heat-treatment scheme was established based on the glass transition temperature (T_g). A systematic investigation of the heat-treatment's effect on the optical properties was conducted on precursor glasses of fixed composition. Considering the actual application of samples, all PLQY measurements were performed using PNCs-glass samples as bulk specimens. As shown in Fig. S2, PLQY of the samples exhibits a trend of initially increasing before decreasing with prolonged heat treatment time. Notably, at the peak PLQY of 72.4%, the emission spectrum displays a narrow full width at half maximum (FWHM) of only 28 nm (Figs. S2(b) and S2(d)), an outstanding achievement for pure-red emission (> 630 nm)[29,30].

Furthermore, we systematically evaluated the PLQY for the entire spectral series of PNCs-glass (Fig. 1(b)). The PNCs-glass samples suitable for RGB primary color applications all exhibit high PLQY values of 72.4% (648 nm), 78.3% (510 nm), and 36.0% (479 nm), respectively (Fig. S3). In particular, PLQY of the pure-blue emitting PNCs-glass reaches the highest value reported to date[31–33]. Fig. 1(c) presents the luminance properties under excitation by a 375 nm UV laser. Our study not only investigates the well-known green-emitting $CsPbBr_3$ glass but also introduces the luminance of pure blue-emitting $CsPb(Cl/Br)_3$ glass. All measurements were conducted on bulk glass samples,

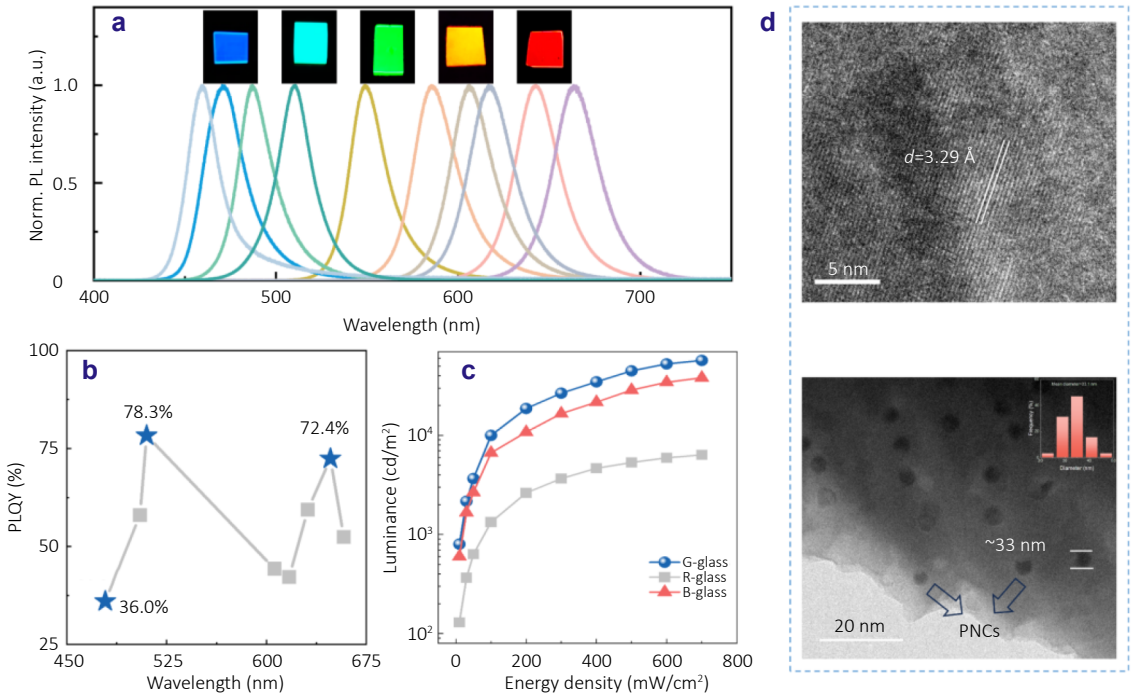


Fig. 1 | (a) PL spectra of PNCs-glasses. Insert: digital photographs of the PNCs-glasses under UV lamp excitation. (b) PLQY of PNCs-glasses. (c) Dependence of the luminance of G-glass, R-glass and B-glass on the excitation power density. (d) TEM images and high-resolution TEM (HRTEM) images of $CsPb(Br/I)_3$@glass.

highlighting their potential for subsequent applications. Luminescence is generally used to define and compare the emission intensity, which is frequently used for electroluminescence and photoluminescence[34–37]. As a result, we also used luminance to clearly show the emission intensity for reasonable comparison. The maximum luminance for $CsPbBr_3$@glass is about 57,100 cd/m^2 with the corresponding excitation power density of 700 mW/cm^2. We extracted a slope efficiency of approximately 8.49 cd/W for G-glass, 0.95 cd/W for B-glass and 5.55 cd/W for R-glass with no obvious roll-off. These key optical performance metrics of these materials (Table S1) show great potential for next-generation display technologies. Transmission electron microscopy (TEM) imaging confirmed the uniform distribution of PNCs within the glass matrix, and the mean diameter is 33.1 nm at 16 mol% F doped. High-resolution TEM (HRTEM) revealed highly crystalline atomic planes with a lattice spacing of 3.29 Å, (1 Å=10^{-10} m) corresponding to the (111) plane of the perovskite structure (Fig. 1(d)). We also statistically analyzed parameters such as the crystal size distribution and spacing under different F doping contents, as shown in Fig. S4 and Table S2. As the NaF content increases, the average PNCs size grows from 12.0 nm to 36.3 nm, and the crystal area fraction rises from 2.0% to 14.8%. This trend indicates that NaF promotes glass-network depolymerization, thereby facilitating the nucleation and growth of PNCs.

The successful formation of PNCs was further corroborated by Raman spectroscopy (Fig. S6), which detected a characteristic peak at ~124 cm^{-1} assigned to the asymmetric stretching mode of the Br-Pb-Br bond[38].

Fluoride has been demonstrated to effectively enhance the performance of perovskite-based optoelectronic devices by passivating defects, increasing the defect formation energy, and suppressing non-radiative recombination pathways[39]. To elucidate the intrinsic mechanism by which F$^-$ ions elevate the optical performance of PNCs-glass, we conducted a series of systematic studies. Fourier Transform infrared spectroscopy (FTIR) (Fig. 2(a)) revealed the impact of F$^-$ incorporation on the borosilicate glass network structure. In the F$^-$-free glass, the absorption band at 1000–1200 cm^{-1} is attributed to the combined stretching vibrations of $[SiO_4]$ and $[BO_4]$ tetrahedral units. With increasing F$^-$ doping concentration, the intensity of this vibrational band gradually decreases. Concurrently, the intensities of the asymmetric (1250–1300 cm^{-1}) and symmetric (1350–1470 cm^{-1}) stretching vibrations associated with $[BO_3]$ trigonal units are enhanced. Additionally, the B-O-B bending vibration at 650–750 cm^{-1} initially strengthens before slightly weakening, while the Si-O-Si bending vibration is observed near 460 cm^{-1} [40–42].

The vibrational modes of boron are considerably more complex than those of silicon due to its dual coordination

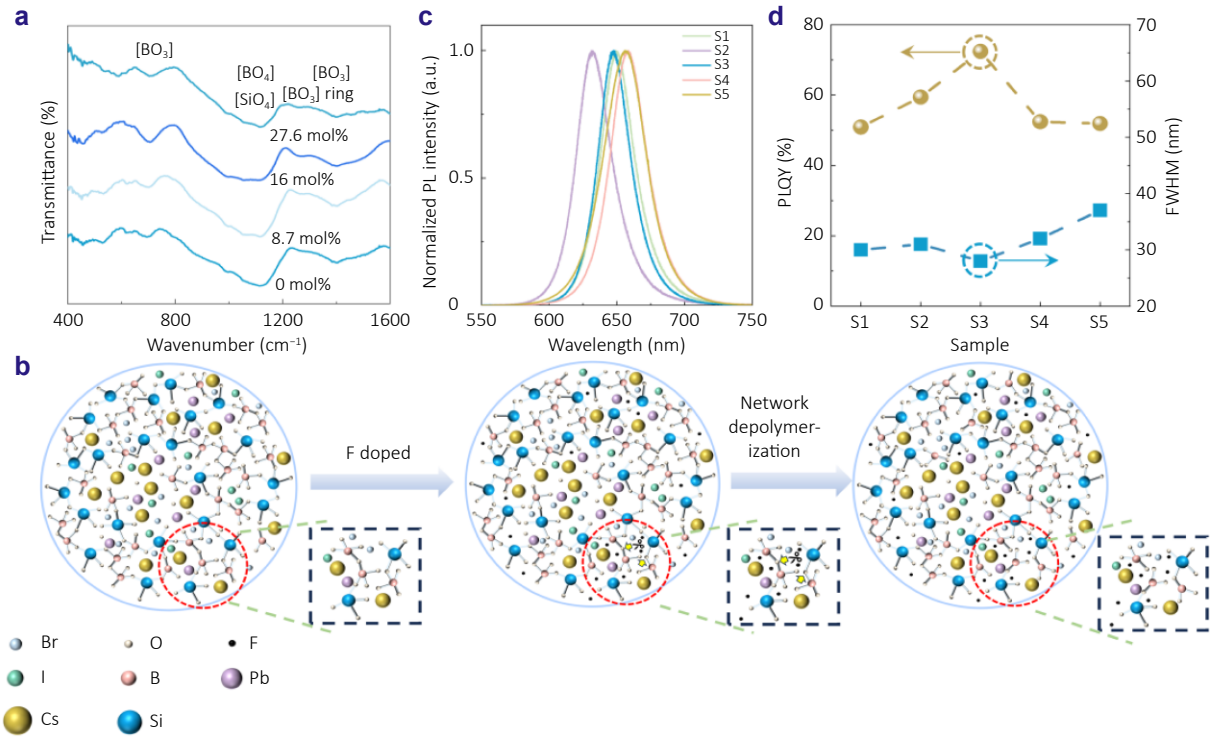


Fig. 2 | (a) FTIR spectra of $CsPb(Br/I)_3$@glass doped with various NaF concentrations (0 mol%, 8.7 mol%, 16 mol%, 27.6 mol%). (b) Schematic diagram of the influence of NaF additive on glass network structure of $CsPbX_3$ PNCs in glass. (c) PL spectra, (d) PLQY & FWHM of $CsPb(Br/I)_3$@glass doped with various NaF concentrations (S1: 0 mol%, S2: 8.7 mol%, S3: 16 mol%, S4: 19.2 mol%, S5: 27.6 mol%).

states as [BO_3] and [BO_4] units. The introduction of F^- alters the equilibrium ratio of these structural units (schematically shown in Fig. 2(b)), promoting the structural transformation from a three-dimensional [BO_4] tetrahedral network to a two-dimensional [BO_3] trigonal unit network. The enhanced strong absorption in the 1200−1500 cm^{-1} region is typically assigned to B-O stretching vibrations in [BO_3] units containing non-bridging oxygens (NBOs). This two-dimensional network structure facilitates the migration and enrichment of Cs^+, Pb^{2+}, and X^- ions, which is essential for the subsequent crystallization of PNCs within the glass precursor.

Generally, active ions (e.g., Cs^+, Pb^{2+}, and halide ions) migration and nanophase separation from the glass matrix are essential for the crystallization of perovskites[21,43]. In the Br^--I^- co-doped glass, Br^- is lighter and smaller than I^-, which leads to faster migration for Br^- from the glass matrix to nanophase separation domains. F^- doping can disrupt the glass network and increase ion migration pathways[44], which allows for promotion of I^- migration and separation. Consequently, more I^- are available for formation of $CsPb(Br/I)_3$, leading to a redshift.

To investigate the influence of F^- on optical properties and to optimize its doping concentration, $CsPb(Cl/Br)_3$@glass and $CsPb(Br/I)_3$@glass were doped with varying levels of F^- (Figs. 2(c), 2(d), and S7). The results demonstrate that as F^- content increases, the PL emission peak exhibits a general redshift, while PLQY first increases and then decreases. This trend is consistent with the carrier lifetime dynamics obtained from time-resolved PL spectroscopy (Fig. S8). The weighted average lifetime first increases and then decreases with the NaF content (rising from 61.8 ns at 0 mol% F doped to 364.5 ns at 16 mol% F doped, and then dropping back to 82.3 ns at 27.6 mol% F doped), and this trend is completely consistent with PLQY. Table S2 shows that F doping increases the crystal size, which leads to a reduction in the specific surface area of PNCs, fewer surface defects, and thus an increase in PL lifetime. However, when F is doped in excess, the nearest-neighbor edge spacing of the crystals becomes too small, which means an increase in reabsorption, resulting in a decrease in PL lifetime.

The luminescence lifetime is in about 30.0 ns for B-glass, 16.2 ns for G-glass and 364.5 ns for R-glass. Under photopic conditions, the sensitivity of human visual system to temporal modulation peaks at 10–20 Hz. Under higher illumination levels, the critical flicker fusion frequency (CFF) can reach approximately 50–60 Hz[45]. In comparison, the fluorescence lifetime of our material is in the range of 10^{-8} to 10^{-7} s. For a display frame rate of 60 Hz, the duration of one frame is about 1.67×10^{-2} s, which is much longer than the fluorescence lifetime, thus preventing perceptible trailing or afterimages between frames.

For the $CsPb(Cl/Br)_3$@glass system, self-crystallization was observed when the F^- doping level reached 2.8 mol%. All PNCs-glass samples feature a narrow FWHM, indicating the formation of high-quality nanocrystals[46]. At 16 mol% F we obtain the narrowest FWHM (28 nm) and the highest PLQY (72.4%). We attribute this to the fact that F promotes the crystallization of the glass. At an F doping concentration of 16 mol%, the crystals exhibit a relatively large size (which implies fewer surface defects), while the self-absorption effect does not increase due to excessively small nearest-neighbor edge spacing—with the spacing being 17.2 nm.

Moreover, the excitonic absorption edge is in close proximity to the PL peak (Fig. S9), resulting in a minimal Stokes shift, which means that the luminescence mainly originates from intrinsic luminescence rather than deep traps. This is consistent with the fact that F doping increases the crystal size and reduces surface defects, thereby improving the crystal quality.

This characteristic is another hallmark of high performance of the materials and is of great significance for the fabrication of high-luminance and high-efficiency light-emitting devices.

Considering that stability is as important as optical performance for practical applications, the PNCs-glasses were subjected to a series of rigorous stability assessments. A critical consideration for mixed-halide perovskites is their inherent instability arising from photo-induced halide segregation, which adversely affects device performance in light-exposed environments[47]. To evaluate this, the PNCs-glasses were subjected to continuous irradiation of 211 W/m^2 by a 405 nm laser for 7 days. As illustrated in Figs. 3(a) and S11, the materials exhibited exceptional photostability, the I/I_0 values of R, G, and B are 96.5%, 98.6%, and 97.1%, respectively (where I and I_0 are the PL intensities after and before UV irradiation, respectively). Additionally, the vertically stacked glass substrates exhibited uniform and stable multi-band luminescence under long-time irradiation with a 405 nm LED at 40 mW/cm^2 (Fig. 3(b)). This result lays a solid foundation for its subsequent application in display devices. The dense inorganic glass separates nanocrystals from the environment, suppresses halide diffusion/segregation, and improves photo-stability under water, heat and UV[48]. When an irradiance of 2.11×10^3 W/m^2 was used in holography, we measured continuous-pump PL and plotted the curve of PL intensity versus time, as shown in Fig. S12. T_{90} is about 50 h for the B layer and >60 h for the R and G layer. Under this pumping condition, the emission color remains stable, peak shift $\Delta\lambda \leq 0.5$ nm, FWHM change ≤ 0.9 nm. The T_{90} of the color shift is greater than 60 h. Upon immersion in ethanol for 90 days, the materials exhibited negligible degradation in their PL intensity, demonstrating excellent chemical resistance (Fig. 3(c)). Furthermore, to assess the performance of the materials under potential temperature fluctuations and light-exposed influence in real-world scenarios, the samples underwent thermal cycling tests by continuous irradiation with a 405 nm laser. As shown in Fig. 3(d), after 10 consecutive heating/cooling cycles between 25 °C and 100 °C, no

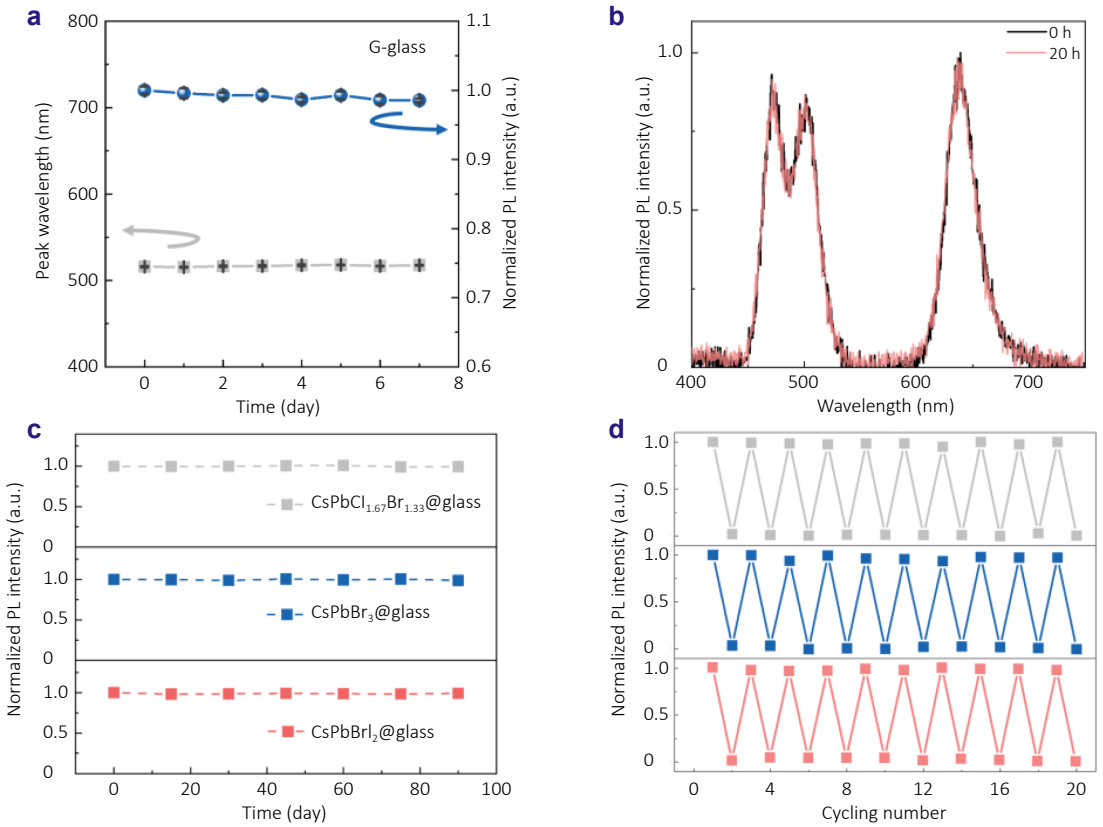


Fig. 3 | Stability of $CsPbCl_{1.67}Br_{1.33}$@glass, $CsPbBr_3$@glass and $CsPbBrI_2$@glass. (a) Normalized PL intensity and peak wavelength of $CsPbBr_3$@glass illuminated for 7 days by 405 nm laser. (b) PL spectra of a vertically stacked PNCs-glass architecture illuminated for 20 h by 360 nm LED. (c) Normalized PL intensity of samples immersed in the ethanol. (d) Under 405 nm UV laser irradiation, normalized PL intensity during thermal cycling measurements between 25 and 100 °C.

significant change in PL intensity was observed, confirming the outstanding thermal endurance of the samples. We previously tested stability for the G layer at 85 °C/53% RH—and the PL intensity retained 98.7% over 90 days (Fig. S13). Collectively, these findings validate that the borosilicate glass matrix provides a robust encapsulation, effectively shielding the embedded PNCs from detrimental external stimuli. This superior protection ensures the long-term stability required for demanding applications.

Leveraging the excellent optical properties and stability demonstrated by the as-prepared materials, we further integrated them with an SLM to explore their potential in advanced display applications. By loading computer-generated holograms (CGHs), the holographic system precisely diffracts a 405 nm CW laser to reconstruct the target optical field, while effectively suppressing stray light in unmodulated regions. This approach resolves the issue of laser speckle, a common artifact that degrades image quality in conventional CGH systems[49,50]. The comparison in Fig. S15 clearly demonstrates the successful elimination of the central zero-order beam and surrounding diffraction noise. Observing the absorption spectrum of the materials, the RGB all exhibit uniformly strong absorption at a wavelength of 405 nm. Meanwhile, no 405 nm peak was observed in the PL spectrum measured with a filter, indicating the absence of pump leakage. For added safety, a 405 nm long-pass filter can be applied to the stacked RGB device to further suppress residual pump light. Therefore, our choice of 405 nm as the pump wavelength is reasonable.

A high fluorescence signal-to-noise ratio (SNR) is another critical factor for achieving high-fidelity patterned displays. On one hand, the high PLQY of the material ensured an intense fluorescence signal; on the other hand, surrounding diffraction noise was minimized via a padded phase map in the unmodulated regions. Consequently, individual pixels remained clearly distinguishable with no significant crosstalk, even when the spacing between adjacent pixels was set to as little as two pixel units. To demonstrate the capabilities of this high-resolution patterning method, we constructed a 100 × 100 close-packed holographic multicolor dot matrix (Fig. S16), achieving a lateral resolution of 0.63 μm per pixel, with a minimum pixel size and pitch reaching ~0.71 μm and ~1.26 μm, respectively. This corresponded to an exceptionally high pixel density of ~20,247 PPI. We also verified the ultra-high resolution through standard imaging metrics. Combining the measurement data of

the USAF resolution target and multi-band modulation transfer function (MTF) data, the calculated pixel density is approximately 2.1×10^4 PPI, which confirms the accuracy of the ultra-high resolution claim. Detailed calculation procedures are provided in Fig. S17.

We constructed a multicolor static display matrix with a tunable wavelength from 460 nm to 650 nm. Fig. 4(a) shows a multicolor display array of 35×35 fluorescent pixels. We compare the PPI in Fig. 4(b). Our pixels are defined by optical addressing, giving an equivalent density of ~2.0×10^4 PPI. Because the RGB layers are addressed at different Z positions, there is no lateral tri-color tiling, so the full-color PPI is the same as the single-color case. Compared with OLED, QLED, PeLED, and printed or photolithographic QD pixels that require side-by-side RGB subpixels, our full-color resolution is markedly higher. It is also at the upper end of what has been reported for single-color micro-displays or single-layer color-conversion samples. Dynamic holographic displays of the letters 'Z', 'J', and 'U' was realized by switching the phase maps (Fig. 4(c)). A comprehensive demonstration of multicolor dynamic holographic displays was presented in supporting videos.

With the pixel spacing set to 4 pixels, the dot matrices remain clearly visible as the array size ranged from 10×10 to 50×50 (Fig. 5). Laser nanofabrication and direct-writing paradigms, where strong optical fields rewrite composition, phase, or morphology in perovskite materials to create persistent or semi-persistent micro/nano structures (materials-level rewrite)[58]. In contrast, our work does not change the local structures of the glass. The pattern is generated entirely by SLM phase holography and turning off the pump or switching phase can immediately remove/rewrite the pattern, with the material state unchanged.

In recent years, emitter and device concepts for high-resolution and high-efficiency displays and holography have developed rapidly. On one hand, high-efficiency backlights and full-color displays based on micro-LEDs, quantum-dot or perovskite color conversion, and lead-free quantum dots have shown clear advantages in brightness, color gamut and process integration[59–61]. On the other hand, new light-field control approaches such as vectorial and metasurface holography have made important progress in multidimensional information encoding and ultrafast dynamic display[62,63]. Building on these advances, we explore multi-color holographic display using an all-inorganic perovskite nanocrystal-in-glass emitting platform combined with a three-dimensional stacked architecture and SLM-based dynamic addressing, aiming at high stability, ultra-high equivalent resolution and a wide color gamut.

In addition, recent progress in orbital-angular-momentum (OAM) and large-capacity holography has further expanded the available design space. Gigapixel digital holography engines and wavelength-OAM multiplexed metasurface holograms have demonstrated extremely high channel

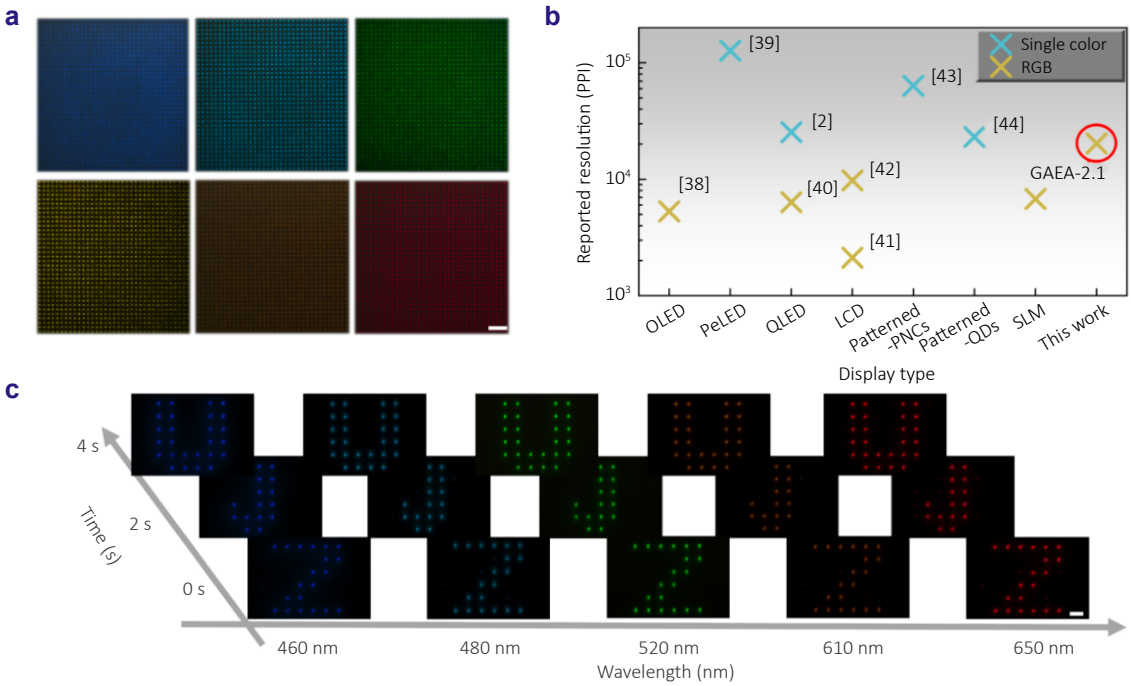


Fig. 4 | (a) Schematic of the high-resolution, holographic multicolor fluorescent dot matrix displays. The displays consist of a 35×35 array with a pitch of 4 pixels between adjacent dots. (b) Comparison of the highest reported resolution for various displays, distinguishing between single-color and RGB displays. The LCD category encompasses both conventional LCDs and liquid crystal on silicon (LCOS) displays. GAEA-2.1 LCOS SLM: pixel pitch = 3.74 μm (≈6,780 PPI)[2,51–57]. (c) Holographic dynamic multicolor displays (460, 480, 520, 610, 650 nm). The excitation wavelength is 405 nm. The scale bar is 10 μm.

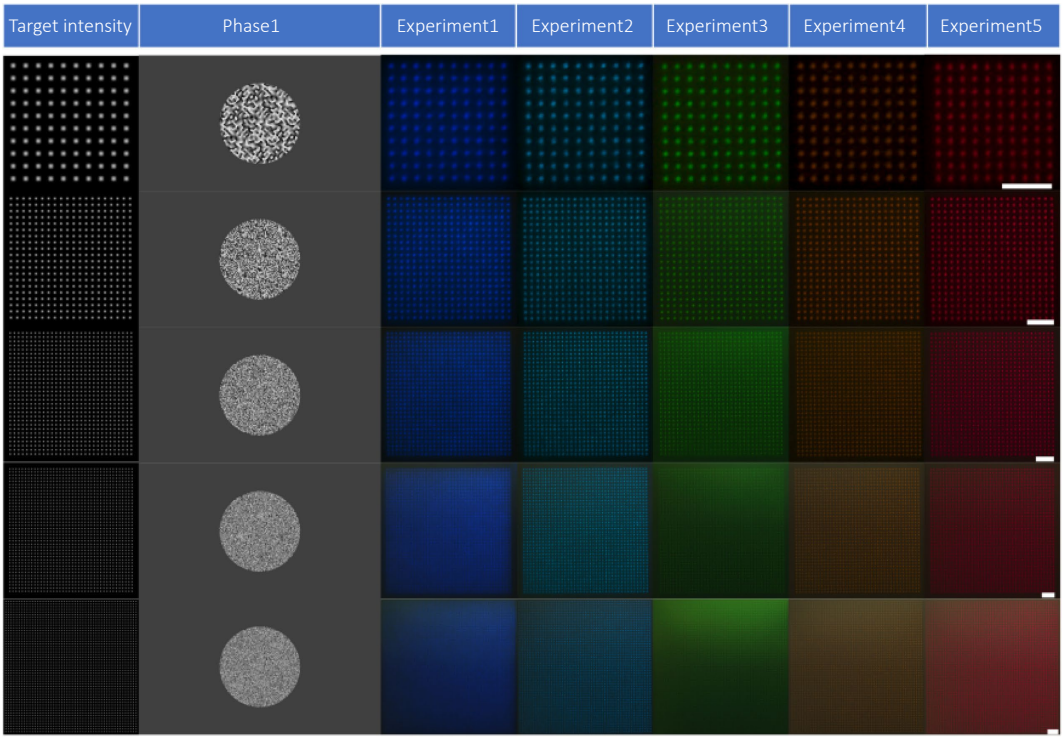


Fig. 5 | Multicolor high-resolution reconstructed display effects as the dot matrix size ranged from 10×10 to 50×50. The pixel spacing was set to 4 pixels. The scale bar is 10 μm.

counts and sharp spectral selectivity for multi-image reconstruction[64,65], while achromatic 3D multi-color OAM holography has shown precise multi-plane, multi-wavelength control within a single compact element[66]. These works highlight the potential of combining advanced wavefront control with high-capacity holographic channels, which is complementary to our materials-driven approach based on stacked perovskite nanocrystal glass and SLM-addressed dynamic holography.

To overcome the inherent limitations of conventional planar pixel layouts in terms of pixel density and spatial utilization efficiency, we innovatively proposed a vertically stacked PNCs-glass architecture. Recent research in image sensors has already confirmed that monolithic vertical stacking is an effective alternative to traditional color filter arrays (CFA)[67]. By transitioning the red (R), green (G), and blue (B) subpixels from a planar arrangement to a spatial stack, the spatial utilization efficiency can be fundamentally increased by a theoretical threefold, enabling much higher pixel densities. The combination of our highly transparent, high-PLQY PNCs-glass, integrated into a vertical stack and addressed by SLM-based holographic projection, paves the way for a low-cost, ultra-high-resolution, and high-fidelity full-color holographic display scheme.

To validate this concept, RGB primary-color PNCs-glasses were cut, polished to the same optical grade, and sequentially stacked. By precisely controlling the focal depth of the excitation light, the PNCs within different layers can be selectively excited. As captured by a CCD camera (Fig. 6(a)), differently colored traffic light patterns were successfully displayed by simply adjusting the focal plane. Owing to the excellent transparency and uniformity of the materials, interlayer interference, such as absorption or scattering of both excitation and emission light, is minimized, ensuring high clarity and fidelity for the resulting patterns. The designed device exhibits superior color reproduction potential for its wide color gamut that covers 112.7% of the NTSC standard, with its corresponding CIE 1931 color coordinates shown in Fig. 6(b). It exceeds representative inkjet-printed QDCC micro-LED prototypes (107.53% NTSC)[68] and is on par with or above many state-of-the-art color-conversion micro-LED implementations (≈110%–114% NTSC)[69,70], and well above pixelated perovskite EL demonstrations (≈102% NTSC)[71].

In addition to microscale multicolor displays, its macroscopic full-color display effects are also clearly visible. The overall system schematic is depicted in Fig. 6(c), where a 405 nm laser is expanded, focused by a single lens (f = 250 mm), and reflected by an SLM (1080 × 1929 resolution, 8 μm pixel pitch) to project directly onto the stacked glass. Fig. 6(d) showcases high-fidelity reconstructions of various color patterns —including pure, mixed, and full-color butterfly images—which faithfully reproduce the details of the original CGHs. There is slight PL leakage that propagates laterally inside the glass during the excitation, which leads to scattering and emitting-like phenomenon when this lateral

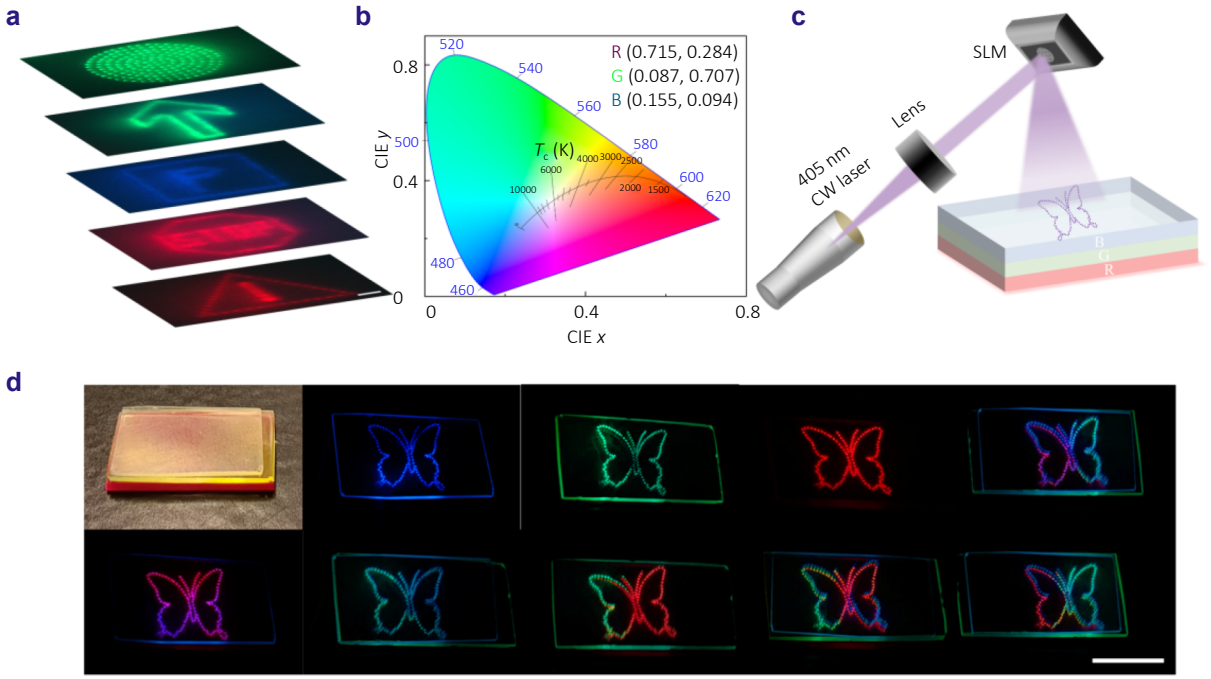


Fig. 6 | (a) Microscopic schematic of the holographic multicolor displays of traffic light patterns, realized by the vertically stacked PNCs-glass architecture. The scale bar is 10 μm. (b) CIE 1931 color gamut diagram for the PNCs-glass, which covers 112.7% of the NTSC standard. (c) Schematic diagram of the display device, which integrates the vertically stacked PNCs-glass structure with an SLM for holographic projection. (d) Macroscopic photographs of the holographic displays, demonstrating tunable full-color emission from the vertically stacked PNCs-glass architecture. The scale bar is 50 mm.

propagating PL reaches the glass–air boundary. Such lateral propagation-induced spill/crosstalk is a known issue in micro-LED displays[72]. In engineering practice, a black/gray photoresist matrix is often used to absorb or stop lateral light, which is also instructive for suppressing our edge glow[72,73]. Considering the optical loss and reabsorption phenomena in the stacked device, we report the optical budget of PL emission, which quantitatively explains the loss distribution in the stacked structure (Fig. S21).

We have also compared our work with other excellent studies. Chen et al.[74] report a TGA decomposition temperature of about 600–650 °C and PL retention for several tens of days in air. Our perovskite nanocrystal glass maintains PL emission intensity for tens of days at 85 °C and under ethanol soaking, and under continuous 405 nm laser irradiation reaches T_{90} of 60 h, 10 thermal cycles also show very good stability. The Chen system uses low-temperature solution-synthesized powders plus resin 3D printing, which is favorable for custom-shaped lighting. Our system uses conventional melt-quench and annealing to form large-area, polishable glass blocks, with good stability, easy stacking, and resolution determined by optical addressing (~2×10^4 PPI equivalent), without per-pixel alignment.

We have also considered the practical production feasibility of the materials. We calculated the Pb content per unit volume in the samples based on the formula and stoichiometric ratio, which are as follows: B: 1.59×10^{-3} mol/cm^3, G: 1.90×10^{-3} mol/cm^3, and R: 1.06×10^{-3} mol/cm^3. Our system is a borosilicate-nanocrystal composite material, where Pb is immobilized in a dense glass network. Borosilicate glass, as the main sequestering phase for Pb-containing substances, has been widely used in nuclear waste management. In the 40-year systematic research on nuclear waste glass, standard water leaching tests were employed to quantitatively characterize the "initial/residual" corrosion rate, demonstrating the long-term safety of "vitrification solidification" for heavy metals[75]. These studies have shown that the glass network can inhibit ion migration over the long term and exhibits excellent long-term durability. Therefore, in end devices, the adoption of structures such as glass-glass lamination, edge-sealing adhesives, or inorganic thin-film barriers can further reduce the risk of environmental release to near the detection limit[75].

The side-by-side pixel arrangement in traditional color displays fundamentally limits their maximum resolution. In contrast, the full-color display resolution of our proposed vertical stack architecture is comparable to that of a monochromatic display, thereby breaking the technological bottleneck where pixel density and color performance are mutually constrained.

3 Conclusions

In conclusion, we have systematically enhanced PLQY of

full-spectrum PNCs-glasses while maintaining high luminance. Notably, PLQY for pure blue emission (< 480 nm) reached a record-high 36% for PNCs-glass composites. Through a series of characterizations, we elucidated the mechanism whereby fluorine doping enhances optical performance by modifying the glass network structure to optimize the behavior and quality of PNCs crystallization. Furthermore, the robust glass matrix provides excellent encapsulation, ensuring the PNCs are highly stable against degradation from ambient light, heat, and chemical solvents. Building upon the exceptional performance of the material for display applications, we integrated the PNCs-glass with an SLM and loaded CGHs, which realized high-resolution holographic multicolor displays with pixel densities up to 20,247 PPI. We further fabricated a full-color, vertically stacked display device that surpasses conventional planar color display technologies in resolution and light utilization efficiency. Considering the future demand for energy-efficient and ultra-high-resolution displays, this work offers a promising new paradigm.

References

1. Yoo J, Lee K, Yang UJ et al. Highly efficient printed quantum dot light-emitting diodes through ultrahigh-definition double-layer transfer printing. *Nat Photon* **18**, 1105–1112 (2024).
2. Meng TT, Zheng YT, Zhao DL et al. Ultrahigh-resolution quantum-dot light-emitting diodes. *Nat Photon* **16**, 297–303 (2022).
3. Nam TW, Kim M, Wang YM et al. Thermodynamic-driven polychromatic quantum dot patterning for light-emitting diodes beyond eye-limiting resolution. *Nat Commun* **11**, 3040 (2020).
4. Yang J, Hahm D, Kim K et al. High-resolution patterning of colloidal quantum dots via non-destructive, light-driven ligand crosslinking. *Nat Commun* **11**, 2874 (2020).
5. Huang YG, Hsiang EL, Deng MY et al. Mini-LED, Micro-LED and OLED displays: present status and future perspectives. *Light Sci Appl* **9**, 105 (2020).
6. Chen HW, Lee JH, Lin BY et al. Liquid crystal display and organic light-emitting diode display: present status and future perspectives. *Light Sci Appl* **7**, 17168 (2018).
7. Ma T, Chen J, Chen ZY et al. Progress in color conversion technology for micro-LED. *Adv Mater Technol* **8**, 2200632 (2023).
8. Luo H, Peng LR, Yang DW et al. Over 30% efficient non-vacuum quantum-dot light-emitting diode with a bi-layer high-precision patternable EGaIn top electrode. *Adv Funct Mater* **35**, 2418868 (2025).
9. Kwon JI, Park G, Lee GH et al. Ultrahigh-resolution full-color perovskite nanocrystal patterning for ultrathin skin-attachable displays. *Sci Adv* **8**, eadd0697 (2022).
10. Luo CZ, Zheng ZS, Ding YH et al. High‐resolution, highly transparent, and efficient quantum dot light‐emitting diodes. *Adv Mater* **35**, 2303329 (2023).
11. Ma T, Wang YF, Chen J et al. One‐step, mask-free, rapid laser writing fabrication of electroluminescent perovskite@oxide pixels for ultra-high PPI, efficient micro‐QLEDs. *Adv Funct Mater* **35**, 2413811 (2025).
12. Lin LH, Dong ZH, Wang J et al. Flexible ultrahigh-resolution quantum-dot light-emitting diodes. *Adv Funct Mater* **34**, 2408604 (2024).
13. Cho H, Pan JA, Wu HQ et al. Direct optical patterning of quantum dot light-emitting diodes via in situ ligand exchange. *Adv Mater* **32**, 2003805 (2020).
14. Cifci OS, Yoder MA, Xu L et al. Luminescent concentrator design for displays with high ambient contrast and efficiency. *Nat Photon* **17**, 872–877 (2023).
15. Ye JZ, Ren AB, Dai LJ et al. Direct linearly polarized electroluminescence from perovskite nanoplatelet superlattices. *Nat Photon* **18**, 586–594 (2024).
16. Ding S, Wang QQ, Gu WC et al. Phase dimensions resolving of efficient and stable perovskite light-emitting diodes at high brightness. *Nat Photon* **18**, 363–370 (2024).
17. Varnakavi N, Velpugonda JL, Lee N et al. In situ synthesis of Br-rich $CsPbBr_3$ nanoplatelets: enhanced stability and high PLQY for wide color gamut displays. *Adv Funct Mater* **35**, 2413320 (2025).
18. Gao Y, Cai QT, He YF et al. Highly efficient blue light-emitting diodes based on mixed-halide perovskites with reduced chlorine defects. *Sci Adv* **10**, eado5645 (2024).
19. Lee S, Kim J, Kim H et al. Brightening deep-blue perovskite light-emitting diodes: a path to Rec. 2020. *Sci Adv* **10**, eadn8465 (2024).
20. Ai B, Liu C, Wang J et al. Precipitation and optical properties of $CsPbBr_3$ quantum dots in phosphate glasses. *J Am Ceram Soc* **99**, 2875–2877 (2016).
21. Sun K, Tan DZ, Fang XY et al. Three-dimensional direct lithography of stable perovskite nanocrystals in glass. *Science* **375**, 307–310 (2022).
22. Gopakumar M, Lee GY, Choi S et al. Full-colour 3D holographic augmented-reality displays with metasurface waveguides. *Nature* **629**, 791–797 (2024).
23. Li J, Li XX, Huang XY et al. High space-bandwidth-product (SBP) hologram carriers toward photorealistic 3D holography. *Laser Photon Rev* **18**, 2301173 (2024).
24. Li XK, Sun K, Wu JJ et al. Thermal-triggered phase separation and ion exchange enables photoluminescence tuning of stable mixed-halide perovskite nanocrystals for dynamic display. *Laser Photon Rev* **18**, 2301244 (2024).
25. Wu JJ, Li XK, Sun K et al. Tight focusing holographic network enables 3D real time and accurate light field modulation. *Laser Photon Rev* **19**, 2401742 (2025).
26. Liu XQ, Xu YS, Zhang XH et al. Surface electric dipole moment engineering of all-inorganic transparent solid matrix for information encryption and X‐ray imaging. *Adv Funct Mater* **35**, 2418032 (2025).
27. Luo JB, Wei JH, Zhang ZZ et al. A melt-quenched luminescent glass of an organic-inorganic manganese halide as a large-area scintillator for radiation detection. *Angew Chem Int Ed* **62**, e202216504 (2023).
28. Chen SC, Guo CL, Chen SC et al. Enhanced stability of melt-processable organic-inorganic hybrid manganese halides for X‐ray imaging. *Small* **20**, 2406032 (2024).
29. Yan MQ, Yang JP, Yang F et al. Elevating red emission: Yb^{3+} doped $CsPbBr_1I_2$ nanocrystal glass for exceptional PLQY and stability in wide color gamut backlit displays. *J Alloys Compd* **1010**, 177034 (2025).
30. Yang BB, Zhu YX, Li WC et al. High-efficiency pure-red perovskite quantum dots glass via Dy modification for high quality backlight display. *J Alloys Compd* **1010**, 177437 (2025).
31. Shen SL, Guo ZY, Zhong WM et al. Regulating the local glass networks to enhance the optical performance of $CsPbX_3$ (X = Cl, Br, I) quantum dots embedded in zinc borosilicate glasses *via* GeO_2. *Chem Eng J* **505**, 159341 (2025).
32. Pang XL, Zhang HR, Xie LQ et al. Precipitating $CsPbBr_3$ quantum dots in boro-germanate glass with a dense structure and inert environment toward highly stable and efficient narrow-band green

emitters for wide-color-gamut liquid crystal displays. *J Mater Chem C* **7**, 13139–13148 (2019).
33. Sun ZQ, Li YX, Bai HW et al. Preparation of F/Mn-doped $CsPb(Br/Cl)_3$ quantum-dot glass and their luminescence properties. *Funct Mater Lett* **17**, 2451034 (2024).
34. Yin YM, Hu ZP, Ali MU et al. Full-color micro-LED display with $CsPbBr_3$ perovskite and CdSe quantum dots as color conversion layers. *Adv Mater Technol* **5**, 2000251 (2020).
35. Deng LW, Zhang X, Yan YG et al. Ambient contrast ratio of quantum-dot color-converted micro-LED displays. *Results in Phys* **48**, 106462 (2023).
36. Chen SX, Lin JD, Huang J et al. $CsPbBr_3$@glass nanocomposite with green-emitting external quantum efficiency of 75% for backlit display. *Adv Funct Mater* **34**, 2309293 (2024).
37. Jing YY, Yao MY, Yang M et al. Photolithographic fabrication of high-resolution Micro-QLEDs towards color-conversion microdisplay. *Light Sci Appl* **14**, 370 (2025).
38. Batignani G, Fumero G, Srimath Kandada AR et al. Probing femtosecond lattice displacement upon photo-carrier generation in lead halide perovskite. *Nat Commun* **9**, 1971 (2018).
39. Zhao XM, Zhang PK, Liu TJ et al. Operationally stable perovskite solar modules enabled by vapor-phase fluoride treatment. *Science* **385**, 433–438 (2024).
40. Pernice P, Esposito S, Aronne A et al. Structure and crystallization behavior of glasses in the BaO-B_2O_3-Al_2O_3 system. *J Non-Cryst Solids* **258**, 1–10 (1999).
41. El-Egili K. Infrared studies of Na_2O-B_2O_3-SiO_2 and Al_2O_3-Na_2O-B_2O_3-SiO_2 glasses. *Phys B Cond Matter* **325**, 340–348 (2003).
42. Zhang K, Zhou DC, Qiu JB et al. Effect of topological structure on photoluminescence of $CsPbBr_3$ quantum dot doped glasses. *J Alloys Compd* **826**, 154111 (2020).
43. Liu C, Huang WT, Liu RS. Stable glass-protected $CsPbX_3$ (X = Cl, Br, and I) perovskite quantum dots and their applications in backlight LED. *Prog Mater Sci* **143**, 101243 (2024).
44. Zheng WY, Wang Z, Chen WL et al. Unlocking high photosensitivity direct laser writing and observing atomic clustering in glass. *Nat Commun* **15**, 8366 (2024).
45. Kelly DH. Visual responses to time-dependent stimuli. I. Amplitude sensitivity measurements. *J Opt Soc Am* **51**, 422–429 (1961).
46. Wang ZQ, Li XK, Chen CD et al. Humidity-assisted high-resolution laser patterning of perovskite nanocrystals on glass beyond the diffraction limit. *Laser Photon Rev* **19**, 2402093 (2025).
47. Mao WX, Hall CR, Bernardi S et al. Light-induced reversal of ion segregation in mixed-halide perovskites. *Nat Mater* **20**, 55–61 (2021).
48. Zheng RL, Ueda J, Shinozaki K et al. Reversible phase segregation and amorphization of mixed-halide perovskite nanocrystals in glass matrices. *J Phys Chem Lett* **13**, 7809–7815 (2022).
49. Dong ZX, Ling YY, Li Y et al. Motion Hologram: Jointly optimized hologram generation and motion planning for photorealistic 3D displays via reinforcement learning. *Sci Adv* **11**, eads9876 (2025).
50. Shi L, Li BC, Kim C et al. Towards real-time photorealistic 3D holography with deep neural networks. *Nature* **591**, 234–239 (2021).
51. Kato K, Kobayashi H, Shishido H et al. 5, 291 - ppi OLED display enabled by monolithic integration of *C* - axis - aligned crystalline IGZO FET and Si CMOS. *J Soc Info Display* **30**, 690–698 (2022).
52. Lian YX, Wang YX, Yuan YC et al. Downscaling micro- and nano-perovskite LEDs. *Nature* **640**, 62–68 (2025).
53. Yang KY, Zheng HX, Zhong C et al. High-resolution and high-performance full-color electroluminescent quantum dot light-emitting diodes. *Nano Energy* **138**, 110817 (2025).
54. Wu YH, Tsai CH, Wu YH et al. Breaking the limits of virtual reality display resolution: the advancements of a 2117-pixels per inch 4K virtual reality liquid crystal display. *J Opt Microsyst* **3**, 041208 (2023).
55. Amari K, Honda T, Sakairi T et al. Novel CMOS-backplane technologies for fine pixel pitch and high image quality of LCOS microdisplay. *Proc Int Disp Workshops* **28**, 173–176 (2021).
56. Zhang QP, Sun XF, Chen GY et al. Pixelation of perovskite quantum wire thin films with 0.18-μm features and 63, 500-ppi pixel density. *Sci Adv* **11**, eadu3840 (2025).
57. Luo CZ, Ding YH, Ren ZW et al. Ultrahigh-resolution, high-fidelity quantum dot pixels patterned by dielectric electrophoretic deposition. *Light Sci Appl* **13**, 273 (2024).
58. Cherepakhin A, Zhizhchenko A, Khmelevskaia D et al. Advanced laser nanofabrication technologies for perovskite photonics. *Adv Opt Mater* **12**, 2302782 (2024).
59. Lai SQ, Liu SB, Li ZL et al. Applications of lasers: a promising route toward low-cost fabrication of high-efficiency full-color micro-LED displays. *Opto-Electron Sci* **2**, 230028 (2023).
60. Lu TW, Lin Y, Zhang TQ et al. Self-polarized RGB device realized by semipolar micro-LEDs and perovskite-in-polymer films for backlight applications. *Opto-Electron Adv* **7**, 230210 (2024).
61. Wu Z, Xu LM, Wang JD et al. Finely regulated luminescent Ag-In-Ga-S quantum dots with green-red dual emission toward white light-emitting diodes. *Opto-Electron Adv* **7**, 240050 (2024).
62. Ye YQ, Pi DP, Gu M et al. Research progress and applications of vectorial holography. *Opto-Electron Eng* **51**, 240082 (2024).
63. Liu YC, Xu K, Fan XH et al. Dynamic interactive bitwise meta-holography with ultra-high computational and display frame rates. *Opto-Electron Adv* **7**, 230108 (2024).
64. Pi DP, Gao L, Ye YQ et al. Direct laser writing 3D carbon dot array for orbital angular momentum holographic encryption. *Laser Photon Rev* **20**, e01648 (2026).
65. Meng WJ, Fröch JE, Cheng K et al. Ultranarrow-linewidth wavelength-vortex metasurface holography. *Sci Adv* **11**, eadt9159 (2025).
66. Su H, Li BL, Bai YK et al. Achromatic 3D multi-color orbital angular momentum holography. *Adv Sci* **12**, 2503488 (2025).
67. Tsarev S, Proniakova D, Liu XQ et al. Vertically stacked monolithic perovskite colour photodetectors. *Nature* **642**, 592–598 (2025).
68. Qin F, Liu C, Wu WH et al. Inkjet printed quantum dots color conversion layers for full-color micro-LED displays. *Electron Mater Lett* **19**, 19–28 (2023).
69. Anwar AR, Sajjad MT, Johar MA et al. Recent progress in micro-LED-based display technologies. *Laser Photon Rev* **16**, 2100427 (2022).
70. Yang CQ, Zhu JH, Huang CC et al. High color purity emission from quantum dots by optimizing the full width at half the maximum and optical density to blue light. *J Soc Inf Disp* **28**, 623–628 (2020).
71. Liu Y, Li FS, Huang W. Perovskite micro-/nanoarchitecture for photonic applications. *Matter* **6**, 3165–3219 (2023).
72. Yin YM, Hu ZP, Ali MU et al. Alleviating the crosstalk effect via a fine-moulded light-blocking matrix for colour-converted micro-LED display with a 122% NTSC gamut. *Light Adv Manuf* **3**, 36 (2022).
73. Chen SWH, Huang YM, Singh KJ et al. Full-color micro-LED display with high color stability using semipolar (20-21) InGaN LEDs and quantum-dot photoresist. *Photon Res* **8**, 630 (2020).
74. Chen YM, Zhu HY, Babaian D et al. Near-unity PLQY of $Cs_3Cu_2X_5$ (X = Cl, Br) for high-efficiency white light-emitting diodes with exceptional color quality. *Adv Mater* **37**, 2500083 (2025).
75. Thorpe CL, Neeway JJ, Pearce CI et al. Forty years of durability assessment of nuclear waste glass by standard methods. *npj Mater Degrad* **5**, 61 (2021).

Acknowledgements

This work was supported by the National Natural Science Foundation of China (Grant No. 62275233) and the Zhejiang Provincial Natural Science Foundation of China (Grant Nos. LR25E020002 and LDG25F050001) and the Opening Project of State Key Laboratory of Advanced Glass Materials.; National Natural

Science Foundation of China (Nos.62405223; 62575219). The authors gratefully acknowledge Zhejiang Lab for providing the instrumentation used in this study.

Author contributions

C.R. performed the experiments, collected the data, and wrote the initial manuscript. X.L., K.S., and J.Q. discussed the manuscript. D.T. conceived the idea, organized, and supervised the project, interpreted the results, and revised the manuscript.

Competing interests

The authors declare no competing interests.

Supplementary information

Supplementary information for this paper is available at
https://doi.org/10.29026/oea.2026.250238

Open Access This article is licensed under a Creative Commons Attribution 4.0 International License, which permits use, sharing, adaptation, distribution and reproduction in any medium or format, as long as you give appropriate credit to the original author(s) and the source, provide a link to the Creative Commons license, and indicate if changes were made. To view a copy of this license, visit
http://creativecommons.org/licenses/by/4.0/
©The Author(s) 2026.
Published by Editorial Office of *Opto-Electronic Advance*, Institute of Optics and Electronics, Chinese Academy of Sciences.

Opto-Electronic Journals Group
www.oejournal.org
Scan for Article PDF